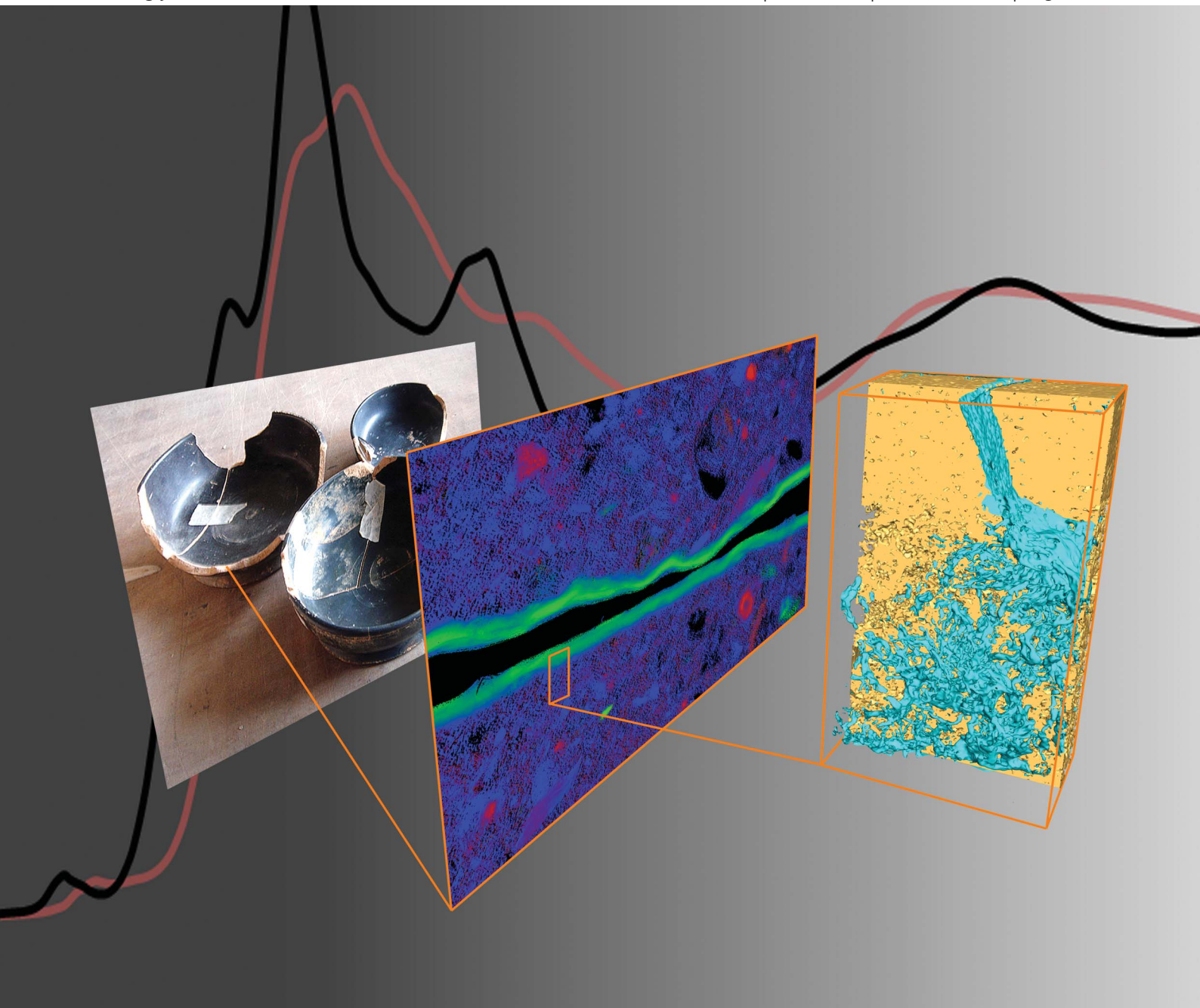


# J A A S

Journal of Analytical Atomic Spectrometry

[www.rsc.org/jaas](http://www.rsc.org/jaas)

Volume 28 | Number 12 | December 2013 | Pages 1807–1952



ISSN 0267-9477

RSC Publishing

**PAPER**

Philippe Sciau *et al.*  
Full-field XANES analysis of Roman ceramics to estimate firing conditions—A novel probe to study hierarchical heterogeneous materials



0267-9477 (2013) 28:12;1-5

# Full-field XANES analysis of Roman ceramics to estimate firing conditions—A novel probe to study hierarchical heterogeneous materials

Cite this: *J. Anal. At. Spectrom.*, 2013, **28**, 1870

Florian Meirer,<sup>a</sup> Yijin Liu,<sup>b</sup> Emeline Pouyet,<sup>c</sup> Barbara Fayard,<sup>c</sup> Marine Cotte,<sup>c</sup> Corinne Sanchez,<sup>d</sup> Joy C. Andrews,<sup>b</sup> Apurva Mehta<sup>b</sup> and Philippe Sciau<sup>\*e</sup>

Roman black gloss ceramics from two different locations and separated by 50–80 years were investigated by X-ray absorption near edge structure analysis in full field hard X-ray transmission microscopes. These spectro-microscopy measurements were complemented by Raman spectroscopy, and X-ray diffraction spot analyses to gain insights into possible differences in manufacturing technology. Our results indicate that the two vessels underwent significantly different firing protocols, suggesting that there was a surprisingly quick evolution of a complex technological process in response to changing needs and tastes of a burgeoning empire. Furthermore, our results show that the ability of the full field X-ray spectro-microscope to investigate large sample areas (from hundreds of  $\mu\text{m}^2$  to as much as  $2\text{ mm}^2$ ) with high spatial resolution (of 300 nm down to 30 nm) together with its ability to correlate sample porosity (derived from tomography) with the distribution of chemical phases makes it an invaluable tool in the investigation of nanoscale processes in hierarchically heterogeneous chemical systems—from Roman ceramics to some of the most advanced technological products of today.

Received 9th July 2013

Accepted 25th September 2013

DOI: 10.1039/c3ja50226k

[www.rsc.org/jaas](http://www.rsc.org/jaas)

## 1 Introduction

Hierarchically complex materials are everywhere. They include modern Li-ion batteries to ancient ceramics. Understanding how they were produced and how they function and fail requires knowledge of nanoscale processes/features that are heterogeneously distributed over tens of microns. Finding them reliably is akin to finding a wooden needle in a haystack and requires a probe with exquisite sensitivity to mineralogical variation, sub-micron resolution, and a field of view (FOV) of hundreds of microns. Until recently no such probe was available. In here, using two Roman black gloss ceramics as examples, we outline a new approach for probing highly heterogeneous materials.

In archaeological investigations, ceramics are advanced technological products. Not only are they identifying markers, but often also indicators of technological prowess of a civilization and/or an archaeological period. Consequently, they have been a major focus of archaeometric research from the beginning of the field in the 1950s.<sup>1</sup>

The iconic red and black ceramics produced from Fe-rich illite clay are associated with the Mediterranean region in the classical period.<sup>2</sup> These black gloss ceramics were first produced in Corinth and Athens in the 6<sup>th</sup> century BCE. The production slowly moved west to central and northern Italy in the 4<sup>th</sup> century BCE and finally to southern Roman France where it disappeared in the early decades of 1<sup>st</sup> century CE. The basic material chemistry of these ceramics was the same throughout its long existence. The glossy black (containing significant amounts of  $\text{Fe}^{2+}$ ) and reds and the ochre ground (composed almost entirely of  $\text{Fe}^{3+}$ ) were produced from clays with very similar bulk chemistry but by manipulation of Fe oxidation state and mineralogy through skilled control of nanoscale porosity, kiln temperatures and oxidative environment.<sup>3–7</sup> Such a precise control of chemistry through porosity is still considered one of the milestones of technological achievement in human history. Though several tens of thousands of fragments of ceramics have survived, the details of the technology that produced them are lost. Since late 18<sup>th</sup> century many different scenarios for the production of “Black Gloss” (BG) ceramics have been proposed. The most commonly accepted, as described by Noble in 1965,<sup>2</sup> is that painted vessels were subjected to a single three-stage (oxidative  $\rightarrow$  reductive  $\rightarrow$  oxidative) firing. However, our understanding of this technology is still sufficiently incomplete that even now many replication attempts result in misfires and poor colour and sheen blacks.

In here, we will show that though the basic Fe redox chemistry appears to have remained constant for over 600 years,

<sup>a</sup>Inorganic Chemistry and Catalysis, Debye Institute for Nanomaterials Science, Utrecht University, Universiteitsweg 99, 3584 CG Utrecht, The Netherlands

<sup>b</sup>SSRL, SLAC, 2575 Sand Hill Road, Menlo Park, CA 94025, USA

<sup>c</sup>ID21, ESRF, BP 220, 38043 Grenoble, France

<sup>d</sup>Archéologie des Sociétés Méditerranéennes, UMR 5140, 390 ave de Pérols, 34970 Lattes, France

<sup>e</sup>CEMES, CNRS, Université de Toulouse, 29 rue J. Marvig, 31055 Toulouse, France. E-mail: [philippe.sciau@cemes.fr](mailto:philippe.sciau@cemes.fr); Fax: +33 562257999; Tel: +33 562257850

subtle changes in mineralogy can be observed, arising from small changes in technology across the region and over time. The mineralogical changes are, therefore, markers of differences in starting clay chemistry and morphology, and small variations in redox chemistry due to intentional changes or accidental fluctuations in the firing temperature and/or the oxygen fugacity. Mapping the mineralogical distribution, therefore, allows reconstruction of some of the lost details of the production technology. However, often the distribution of key minerals is heterogeneous and frequently confined to near surface regions and the small interfacial region between the slip and the body requires a characterization probe designed for hierarchically heterogeneous materials.

Combination of two different advances in X-ray science; high resolution microscopy with X-ray spectroscopy, has for the first time provided a probe capable of investigating small and subtle oxidation state and mineralogy variations in highly heterogeneous materials, such as the two Roman black gloss ceramics of interest to this investigation. The position and shape of an absorption edge as measured in X-ray absorption near edge structure (XANES) analysis contains not only information about the oxidation state of the element of interest, but is often a unique signature of the mineral phase it is contained in. It is, therefore, increasingly used for studies of ceramics with multiple oxidation states and diverse mineralogy. In 2011, at SSRL, a zone plate based full-field transmission X-ray microscope (TXM) at SSRL with a FOV of  $30\ \mu\text{m}^2$  and a resolution of 30 nm (ref. 8–10) was combined with XANES analysis. This development was shortly followed by the implementation of XANES analysis on another (lens less) full-field microscope at the ESRF with a FOV from  $600\ \mu\text{m}^2$  up to  $2\ \text{mm}^2$  and resolutions ranging from 0.3 to  $1.4\ \mu\text{m}$ .<sup>11,12</sup> In this investigation we used both of these microscopes.

## 2 Samples and archaeological background

For this study, we selected two fragments of roman ceramics, from two different locations and times, which were fired using the B-protocol of Picon's nomenclature, *i.e.*, with a reducing heating followed by an oxidizing cooling.<sup>13</sup> The first one (reference CABNarb-B) is a B type Campanian ceramic: it has a high black gloss coating with a red non-vitrified body. It was found during the excavations of the old city of Narbonne and it is dated to the 1<sup>st</sup> cent BCE. This sherd was associated with a set of Campanian ceramic plates, and thought to be broken when a box containing them was dropped during unloading. Therefore, the ceramic was never used and belongs to a homogeneous group, maybe of Etruscan origin.

The second sample (PTSGD17-H) is a fragment of Pre-sigilata made at the La Graufesenque workshop (Millau, France).<sup>7,14</sup> Its paste is non-vitrified and has a red/brown colour while its slip is black. The slip is vitrified but not as brilliant as that of the Campanian sample. This sherd was found during the excavation of a dump site called "cendrier", dating back to the Augustan period.<sup>15</sup> It belongs to the imitations of the service II plates (Drag. 17), which are a typical form of the La Graufesenque production from 10 BCE to CE 10. It was previously

analysed at lower resolution and mineralogical sensitivity and those results were published in ref. 6 and 16.

## 3 Experimental details

### 3.1 Sample preparation

Thin cross-sections of the samples were obtained using a method derived for study of materials in a transmission electron microscopy.<sup>17</sup> Sections of two sherds were cut ( $3 \times 10 \times 5\ \text{mm}^3$ ) and glued (Gatan G-1 epoxy) together facing each other to form a sandwich, and thus protecting the two surfaces with black gloss slip from damage. The sandwich was then cut into a  $\sim 300\ \mu\text{m}$  slice, which was subsequently polished down to a final thickness of 40–60  $\mu\text{m}$  by mechanical grinding using SiC and diamond papers (Fig. 1).

### 3.2 Hard X-ray full-field XANES analysis

A few recent studies have highlighted the utility of performing X-ray absorption spectroscopy, in particular X-ray absorption near edge structure (XANES) analysis, in a hard X-ray full field microscope for chemically complex materials.<sup>9,11,18</sup> In this approach,<sup>9</sup> a full-field transmission image is recorded at more than 100 different energies while the energy is tuned in small steps (0.3–10 eV) across the absorption edge of a specific element of interest in the sample. After data pre-processing, which includes image alignment and corrections for sample jitter and possible magnification changes at different energies caused by the X-ray optics, the full field XANES data set represents a 3D radiography stack consisting of more than 100 images recorded at different energies. Therefore, each pixel, of more than a  $1000 \times 1000$  pixel image, contains a full high resolution XANES measurement. This development was also a

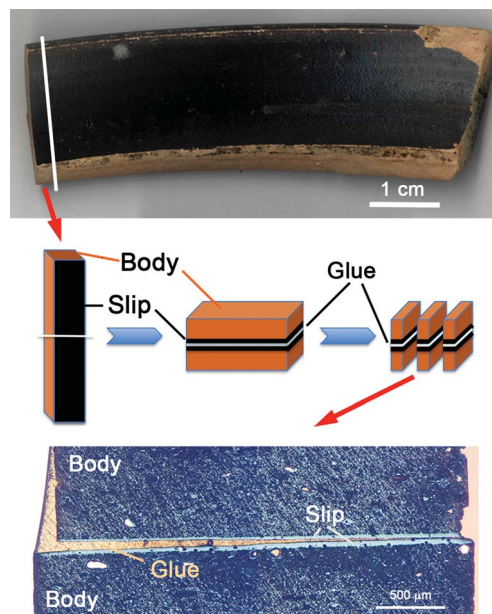


**Fig. 1** Schematic representation of TXM sample preparation from the sherd to the thin plate observed in optical microscopy.



game changer for the analysis of XANES because suddenly the number of X-ray absorption spectra collected within 0.5 to 2 hours changed by several orders of magnitude; from no more than a few hundred in traditional scanning microscopy to more than several million in a mosaic full-field TXM-XANES measurement. Processing that many XANES poses an analytical and computational challenge, but on the other hand it opens up the possibility of finding trace phases and subtle variations *via* application of powerful multivariate analysis, and other search methods developed for the evaluation of similar large datasets (*cf.* Section 3.2.3). To tackle these challenges and opportunities a new software package (TXM-Wizard) was developed<sup>19</sup> (which is freely available for non-commercial use) and used for the analysis of the data presented in this paper.

**3.2.1 SSRL BL 6-2c.** Part of the full-field TXM measurements were performed at the wiggler beamline 6-2 at the Stanford Synchrotron Radiation Lightsource (SSRL), SLAC National Accelerator Laboratory.<sup>8</sup> The setup consists of a LN<sub>2</sub> cooled, fixed-exit double-crystal monochromator equipped with both Si(111) and Si(311) crystals to tune the beam energy and the X-ray microscope optimized for photon energies in the range of 5 to 14 keV with spatial and energy resolutions of 30 nm and  $\Delta E/E = \sim 10^{-5}$  (Si(111) crystal), respectively. The microscope achieves a single flat FOV of about  $15 \times 15 \mu\text{m}^2$  or  $30 \times 30 \mu\text{m}^2$  (dependent on the optics used). In this work two sets of experimental parameters were used, mainly accounting for differences in absorption (Fe concentrations) in the two samples. The experimental parameters are reported in Table 1. 2D XANES images were collected with varying energy intervals, with a spectral sampling of 0.5 or 0.25 eV in the immediate Fe K-edge (7112 eV) region using the Si(111) monochromator crystal. This was done to have sufficient energy resolution at the energies where the main XANES features were expected (*e.g.* the white line and the first oscillations that follow) while optimizing measurement time by collecting fewer points using larger energy intervals above and below this region needed for normalization. The scans covered an energy range from about 50 eV below to about 130 eV above the Fe K absorption edge (Table 1). Because the 30 nm resolution of the microscope is achieved by using a zone plate, which is a chromatic optical

element, the zone plate is automatically moved to refocus at every energy point to keep the sample in focus during the entire scan. A set of reference images without the sample was recorded at every energy (using the same experimental parameters) to account for changes in photon flux and small beam instabilities. The transmission images were normalized by the reference images collected at the corresponding energies. A more detailed description of the XANES mode of the full-field TXM at SSRL BL 6-2c can be found elsewhere.<sup>9,19</sup>

**3.2.2 ESRF beamline ID 21.** Full-field measurements with even larger FOV were performed at the new ID21 XANES full-field end-station at the European Synchrotron Radiation Facility (ESRF), Grenoble, France. This end-station is based on a lensless approach, operating between 2 and 9 keV. It achieves a pixel size between 0.3 and  $1.4 \mu\text{m}$  and covers a field of view from  $600 \times 800 \mu\text{m}^2$  up to  $1 \times 2 \text{mm}^2$  within a single frame.<sup>11,12</sup>

The setup consists of a fixed-exit double-crystal monochromator equipped with both Si(111) and Si(220) crystals to tune the beam energy, and an X-ray decoheror (graphite foil,  $125 \mu\text{m}$  thick) to blend the spatial features of the incoming X-ray beam. A 2D detector consisting of a CCD camera coupled to an X-ray scintillator (LSO:Tb type,  $10 \mu\text{m}$ ) and magnifying visible light optics ( $10\times$  or  $20\times$ ) is used to acquire magnified 2D transmission images of the sample at each energy step of the full XANES scan across a given K- or L-edge. As described in paragraph 3.2.1 a reference image recorded with the sample moved out of the X-ray beam is used for intensity normalization. More details of the experimental setup and full-field XANES measurements at ID21 can be found elsewhere.<sup>11</sup> The measurements for the results reported here were recorded using the Si(220) monochromator ( $\Delta E/E = 4 \times 10^{-5}$ ), and an energy step size of 0.3 eV in the immediate Fe K-edge (7112 eV). (See Table 1 for details of data acquisition.) In-house software was developed to optimize the image alignment procedure and, together with handling and processing features for full field XANES stacks, was included in the open source software package PyMca.<sup>20</sup>

**3.2.3 TXM-XANES principal component analysis and clustering.** Two independent approaches were used for a closer inspection of the large XANES data sets: (a) principle component

**Table 1** Experimental parameters used for TXM-XANES imaging at SSRL beamline 6-2c and ESRF beamline ID21. The total exposure time is defined as the exposure time for a single recorded image multiplied by the number of repetitions performed at each energy

Sample	Number of images per XANES scan	Energy range (eV)	Smallest energy step (eV)	Total exposure time (s)
PTSGD17-H	146	7050–7250	0.5	5
CABNarb-B, SSRL	188	7080–7225	0.25	10
CABNarb-B, ESRF	380	7098–7257	0.2	2.1
Sample	Camera binning/ image size	FOV ( $\mu\text{m}^2$ )	Pixel size ( $\mu\text{m}$ )	Total scan time for a single FOV
PTSGD17-H	$2/1024 \times 1024$ pixels	$14.2 \times 14.2$	0.0139	30 min
CABNarb-B, SSRL	$2/1024 \times 1024$ pixels	$29.2 \times 29.2$	0.0285	76 min
CABNarb-B, ESRF	$2032 \times 1036$ pixels <sup>a</sup>	$610 \times 311$	0.3	55 min

<sup>a</sup> At ESRF ID21 no camera binning was used.

analysis (PCA)<sup>21–23</sup> and subsequent *k*-means clustering<sup>24,25</sup> and, (b) least squares linear combination (LSLC) fitting with probable standards and subsequent *R*-factor correlation analysis. Details of the latter approach and how it was applied to the surface tile of zone 1 displayed in Fig. 2 can be found in ref. 19. Using this approach it was possible to identify a very small metallic (Fe<sup>0</sup>) grain (~1 micron), which was most probably stuck in the slip surface during the cleaning phase (zone 1, Fig. 2).

PCA using singular value decomposition (SVD) of the mean centered data matrix (consisting of *p* pixels and *E* energies) was used to reduce its dimensionality from *E* to *N* dimensions by expressing the data set using only the first *N* principal components (PCs). This can be done without losing significant information because the first *N* principal components explain most of the data's variance. Additionally, because the PCs are oriented to best describe the spread in the data, projecting the latter to the *N*-dimensional principal component space ('score plot') highlights the pattern explained by the captured variance and effectively reduces noise, which is now described by PCs having indices larger than *N*. The distance between data points in the score plot is a direct measure of the similarity of the XANES, *i.e.*, the chemical phase, and can be used to cluster pixels according to their (Euclidean) distances from cluster centers (centroid linkage method, *k*-means clustering). As a result, pixels with

similar XANES are effectively clustered into *k* groups resulting in an image segmentation like the one shown in Fig. 3 and 7, for example. The number of clusters *k* has to be at least equal to *N* (here 2) in order to exploit all the information provided by the reduced PC space, but the data was intentionally over-clustered using *k* = 6 to achieve finer image segmentation and interactive curation. A more detailed description of this approach to process full-field TXM-XANES data can be found in ref. 23.

**3.2.4 Full field transmission X-ray tomography.** In order to correlate the (2D) distribution of the different chemical species and the (3D) structure of the Campanian sample, a tomography scan using a range from  $-80^\circ$  to  $80^\circ$  with an angular increment of  $1^\circ$  was performed at BL 6-2c. Furthermore, in order to obtain the 3D distribution of iron in the analyzed volume, the tomographic scans were performed at two energies, one above (7260 eV) and one below (7050 eV) the Fe K-edge.<sup>26</sup> A raster scan of the sample with user defined overlap of the adjacent tiles for better stitching of the projection images (mosaic mode) was performed at each viewing angle to cover a region of interest larger than the available FOV. The Filtered Back-Projection (FBP) algorithm was implemented to retrieve a 3D representation of the sample. Elemental sensitivity to the element of interest (Fe) was achieved by subtracting the images collected at 7050 eV from those collected at 7260 eV.<sup>26</sup>

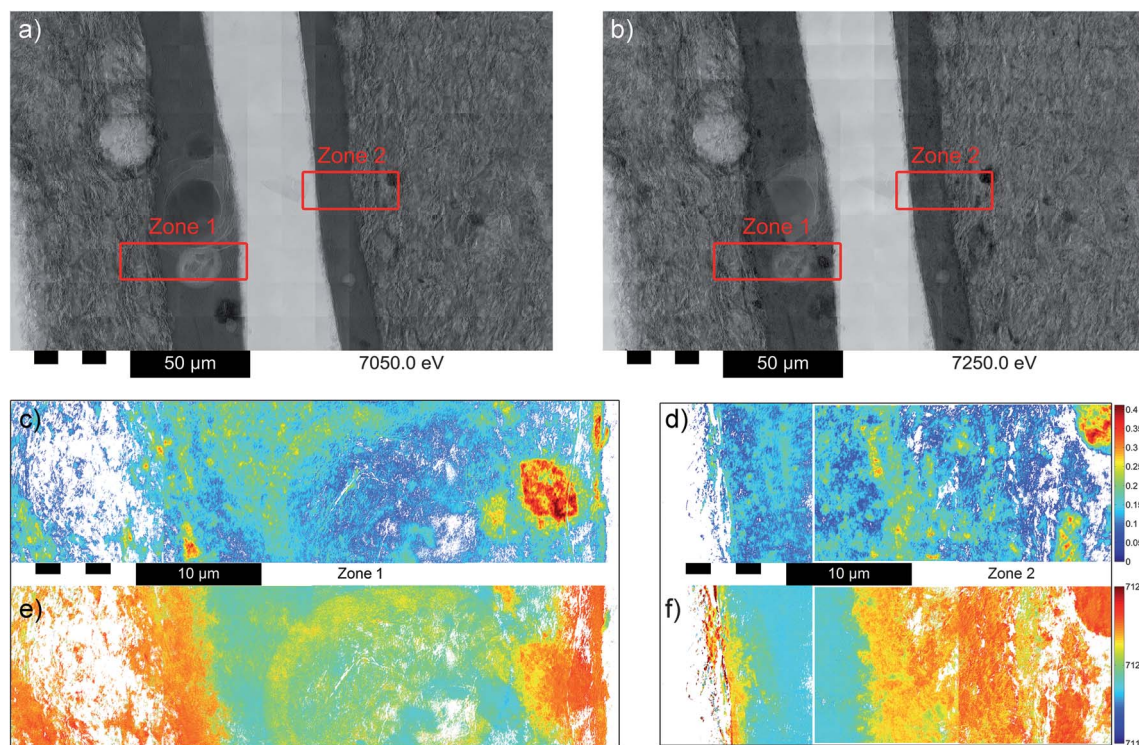


**Fig. 2** Transmission images recorded at (a) 7050 eV, *i.e.*, below the Fe absorption edge and (b) 7250 eV, *i.e.*, above the Fe absorption edge for the Pre-sigillata sample. Both images were collected at SSRL beamline 6-2c in mosaic mode putting together 160 ( $16 \times 10$ ) images with a FOV of  $14.2 \times 14.2 \mu\text{m}^2$  resulting in a total FOV of  $227 \times 142 \mu\text{m}^2$  ( $8192 \times 5120$  pixels, binning 4). The red rectangles, labelled zone 1 and zone 2, designate areas investigated by TXM-XANES analysis. (FOV zone 1:  $3478 \times 929$  pixels or  $48.34 \times 12.91 \mu\text{m}^2$ , binning 2; FOV zone 2:  $2579 \times 912$  pixels or  $35.84 \times 12.68 \mu\text{m}^2$ , binning 2.) Based on the XANES evaluation the edge-jump maps (displayed in (c) and (d)) and corresponding to the Fe concentration as well as the edge energy maps (displayed in (e) and (f)) and correlated to the Fe valence) have been calculated. The scale bar for (c) and (d) reports the values of the (absorption) edge jump, defined as the difference between the average intensity value in the XANES post-edge region and the average intensity value in the XANES pre-edge region. The scale bar for the maps shown in (e) and (f) indicates the energy of the (absorption) edge in eV.

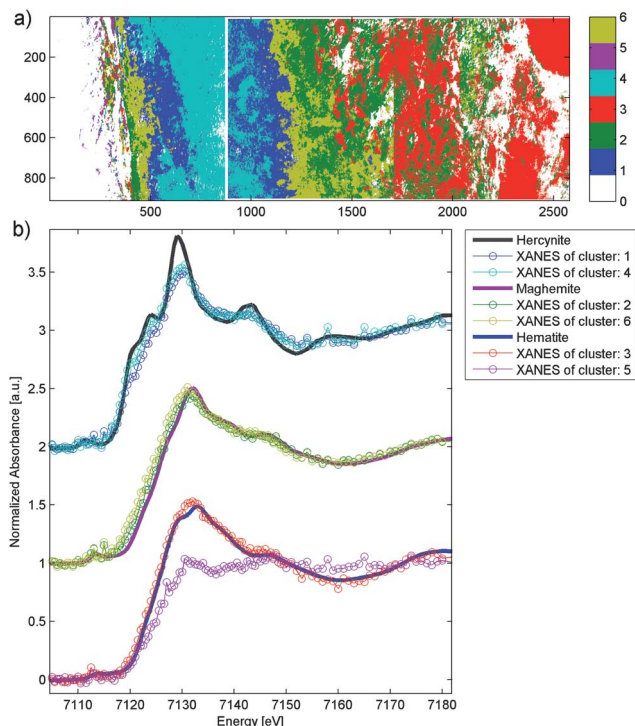


**Fig. 3** (a) Result of the image segmentation based on PCA and *k*-means clustering of zone 2 of the Pre-sigillata sample. The average XANES of each cluster is displayed in (b) together with reference XANES for hercynite, maghemite, and hematite. (Data collected at SSRL beamline 6-2c; FOV zone 2: 2579 × 912 pixels or 35.84 × 12.68 μm<sup>2</sup>, binning 2.)

### 3.3 X-ray diffraction and Raman microspectrometry

Micro-X-ray powder diffraction measurements were carried out on a Bruker D8 Advance device in Bragg–Brentano geometry, equipped with 15 cm long and 100 μm in diameter optical fiber and a fast LynxEye detector. A Cu point focus anode was used to produce X-rays at the characteristic Cu fluorescence lines. Diffraction patterns were acquired between 15 and 60° 2θ with a step size of 0.03° 2θ and a counting time of 200 s per step.

Raman spectra were recorded using an XploRA (HORIBA Jobin Yvon) spectrometer equipped with a Peltier-cooled charge-coupled device (CCD) detector. A 532 nm laser excitation was used and the laser power on the sample was limited to 1 mW. A 100× microscope objective was employed to focus the laser beam to 1 μm (diameter) spot. Wavenumber calibration was regularly verified by measuring the position of the 520 cm<sup>−1</sup> Raman peak from a silicon reference crystal.

## 4 Results and discussion

### 4.1 Sigillata sherd

The body and slip regions of the sherd were analyzed (Fig. 2) using the TXM at SSRL. In order to capture the variation and heterogeneity that is representative of the whole sherd, 160 15 × 15 μm<sup>2</sup> tiles were collected in mosaic mode and stitched together covering a large area of the sample while preserving the high resolution of the microscope.<sup>8</sup> From this large area, two smaller regions were selected for further TXM-XANES

measurements. From the analysis of the XANES for every pixel three important features were extracted *ad hoc*: The transmission map below the Fe K edge (7050 eV), which indicated that the slip is significantly more homogeneous and denser than the body (Fig. 2a). The edge jump maps (Fig. 2c and d) showing the variation of iron concentration, and the edge energy position, which gave information on the oxidation state of iron<sup>9,19</sup> (Fig. 2e and f). In Fig. 2d and f some pixels are missing between the left and middle tile of the 3 × 1 mosaic because the overlap between tiles was not chosen to be sufficiently large to compensate for sample movement and magnification changes during the energy scan. To avoid this in subsequent measurements the overlap was increased accordingly.

The edge jump map does not show a large Fe variation between the slip and the body, which is consistent with the previous electron microprobe quantitative elemental analysis on this sample that shows insignificant difference in the average iron concentration between the slip (4.9 wt%, measured as weight% of iron oxide) and the body (5.4 wt%).<sup>16</sup> However, the TXM edge jump map, does show a distinctly Fe enriched interfacial layer between the slip and the body. We believe that this enrichment is due to a smoothing of the surface of the vase before engobing, during which the fine particles (mainly iron hydroxide, iron oxide and mineral clay) rise to the surface, while the larger particles (of calcite, quartz, feldspar, *etc.*) are buried. In contrast to the Fe concentration (*i.e.*, the Fe K-edge jump), the oxidation state of Fe (as reflected in the position of the Fe K-edge) is distinctly different between body and most of the slip (Fig. 2c and d). In the body, the iron is mainly trivalent whereas it is bivalent in the core of the slip. Fe<sup>3+</sup> is also present at the surface of the slip.

These results are consistent with the results obtained by micro-XANES analysis in X-ray fluorescence (XRF) mode on another fragment from the same vessel.<sup>6</sup> However, the absence of self-absorption effects in the TXM XANES spectroscopy in addition to the much higher spatial resolution of the TXM (~2 orders of magnitude) not only shows a thin, but distinct oxidation layer on the surface of the slip, but also allows a more detailed analysis of the variation in the mineralogy of both the oxidized and reduced Fe oxides.

PCA of the data set collected for zone 2 of the more than 1.76 million XANES showed that using the first two principal components (PC) covering more than 46% of the data's variance is sufficient to perform effective image segmentation by *k*-means clustering in this 2-dimensional PC space. The scores were clustered into 6 groups and the spatial distribution of each of the clusters is plotted in Fig. 3a. The result clearly show that cluster 5 contains only pixels at the very surface of the sample. Further, detailed examination of the XANES of the clusters shows that the XANES of these pixels all have a very small edge jump (very low Fe concentration) and relatively high noise. Therefore, cluster 5 was ignored in the subsequent analysis containing only a very small fraction of the data. On the other hand, the XANES of clusters 1–4 and 6 show clear spectral differences. They were matched against a library of reference XANES of iron oxide minerals from the ALS database, namely one Fe<sup>2+</sup> reference (hercynite (FeAl<sub>2</sub>O<sub>4</sub>)), and two Fe<sup>3+</sup> references (maghemite (γ-Fe<sub>2</sub>O<sub>3</sub>), and hematite (α-Fe<sub>2</sub>O<sub>3</sub>)), respectively.



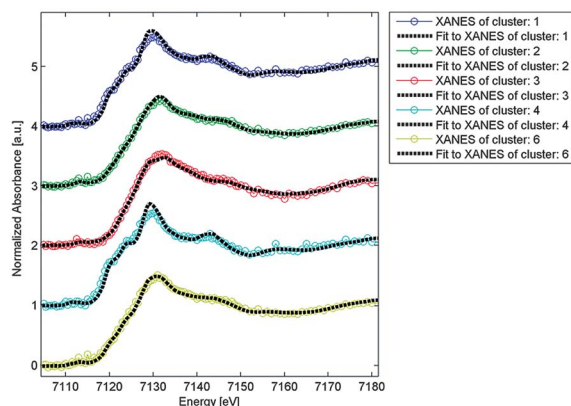


**Fig. 4** Result of a least squares linear combination fit of reference XANES for hercynite, hematite, and maghemite to the XANES of clusters 1–4 and 6 resulting from PCA and *k*-means clustering performed for zone 2 of the Pre-sigillata sample.

The similarity of clusters 1 and 4 with hercynite, clusters 2 and 6 with maghemite, and cluster 3 with hematite is striking (Fig. 3b).

In order to quantify this similarity LSLC fitting of maghemite, hercynite, and hematite references to the XANES of clusters 1–4 and 6 was performed (Fig. 4a) and the results reported in Table 2. The result suggests the absence of hematite in the core of the slip (clusters 1 and 4) and an increasing concentration of hercynite along with a decreasing concentration of maghemite when going from the surface or the body towards the core of the slip (Fig. 4b). The quality of each LC fit can be checked using the *R*-factor commonly used for XANES fitting and defined as:<sup>27</sup>

$$R = \frac{\sum(\text{data} - \text{fit})^2}{\sum(\text{data})^2}$$

The *R*-square value denotes the sum of the squared residuals (sum of squared errors) for each fit. The reduced chi-square (*R*-square divided by the number of degrees of freedom) and the fit errors are calculated in the same way as performed by the FEFFIT program<sup>28</sup> and described in the program documentation.†

LSLC fitting of each single pixel XANES for both zones (7 tiles, containing almost 5 million spectra) was carried out. The result of the fitting is shown in Fig. 5. The single pixel XANES from the core of the slip are very similar to pure hercynite ( $\text{FeAl}_2\text{O}_4$ ) while the body is mainly hematite ( $\alpha\text{-Fe}_2\text{O}_3$ ). This is again in accordance with a previous micro-XAS study performed in XRF mode which revealed that the XANES recorded in the body were most similar to the hematite reference spectrum while the ones recorded in the slip were close to the hercynite reference spectrum.<sup>6</sup> However, the much smaller pixel size used in this study revealed the presence of maghemite ( $\gamma\text{-Fe}_2\text{O}_3$ ) in the slip surface and at the slip/body interface, which was missed in the lower resolution and self-absorbed fluorescence X-ray microprobe XANES measurements. Further statistical analysis

of the LSLC XANES fitting, with *R*-factor correlation analysis first introduced in ref. 19, indicated the need for an additional reference spectrum, namely that of metallic iron ( $\text{Fe}^0$ ), in a small surface grain at the slip surface of zone 1 (Fig. 5c) and the high spatial resolution even allowed seeing that this grain is slightly oxidized at its surface. The small metallic iron surface grain is probably a contaminant, but the presence of maghemite at the surface and the slip-body boundary can be an important signature for the re-oxidation condition undergone by the vessel (see discussion below).

The detection of the highly confined maghemite phase, and especially the small metallic Fe particle are excellent examples for the capabilities of full-field TXM-XANES imaging. The combination of high spatial resolution, large FOV, and full XANES scans for each pixel allows applying statistical methods capable of finding unknown chemical phases confined in very small parts of a large investigated area of the sample. Here it has to be noted that finding unknown chemical phases is only possible when full XANES scans are performed, *i.e.*, energy scans with a sufficient number of energies (typically more than 100) and energy resolution (typically better than 0.5 eV). Finally, such statistical analyses are powerful to support the decision which reference XANES spectra should be used in the final LSLC fitting of the whole dataset. Usually such decisions require *a priori* knowledge about the chemical phases present in the sample and unknown phases, especially those present in small concentrations or areas, are easily missed.

## 4.2 Campanian sherd

**4.2.1 Full-field TXM XANES at SSRL.** The same approach was applied to the Campanian sample (CABNarb-B). Fig. 6 shows the transmission image recorded at 7225 eV (Fig. 6a), the edge jump (Fig. 6b), the edge energy position map (Fig. 6c) and the phase map (Fig. 6d). The edge jump map shows that in this sample, as opposed to the Pre-sigillata sample, the slip contains significantly more and homogeneously distributed Fe than the body. This is again in agreement with microprobe analysis, which revealed that the slip of this Campanian ceramic contains 13.4% Fe (measured as weight% of iron oxide) while the Fe concentration in the body is, similar to that of the Pre-sigillata sample, around 6.7% (oxide wt). The edge energy position map shows the same general behavior as observed for the Pre-sigillata sample, *i.e.*, the iron is mainly trivalent in the body and bivalent in the slip. However, unlike the Pre-sigillata sample, no oxidized iron layer is observed on the slip surface.

PCA of the more than 1.75 million XANES of this data set was performed keeping the first 2 PC covering 70% of the data's variance. Subsequent *k*-means clustering in 2 dimensional PC space using 6 clusters produced efficient image segmentation as displayed in Fig. 7a. The XANES of clusters 1–6 and the reference XANES of hercynite, maghemite, and hematite are reported in Fig. 7b, clearly showing that the XANES data suggests the presence of only two mineral phases in the CABNarb-B sample, namely hercynite and maghemite.

The distribution of the clusters shows a distinct phase transformation from hercynite in the slip to maghemite in the

† M. Newville, FEFFIT – Using FEFF to model XAFS data, *Goodness of Fit and Uncertainties in the Variables*, 1998, ch. 5, downloaded April 1st 2012 from <http://cars9.uchicago.edu/~newville/feffit/>.

**Table 2** Least squares linear combination fit results for clusters 1–4, and 6 from PCA and *k*-means clustering of the data collected for zone 2 of the sample PTSGD17-H (Fig. 3 and 4). Clusters (Clt) have been sorted according to increasing maghemite concentrations

	Hercynite	Hematite	Maghemite	<i>R</i> -square	<i>R</i> -factor	Reduced chi-square
Clt 2	0.18 (1)	0.00 (6)	0.82 (6)	0.091	0.009	0.0006
Clt 6	0.34 (1)	0.13 (7)	0.53 (7)	0.123	0.001	0.0009
Clt 1	0.62 (2)	0.00 (9)	0.38 (9)	0.229	0.002	0.0016
Clt 4	0.81 (2)	0.00 (12)	0.20 (12)	0.415	0.003	0.0029
Clt 3	0.09 (1)	0.82 (6)	0.09 (7)	0.117	0.001	0.0008

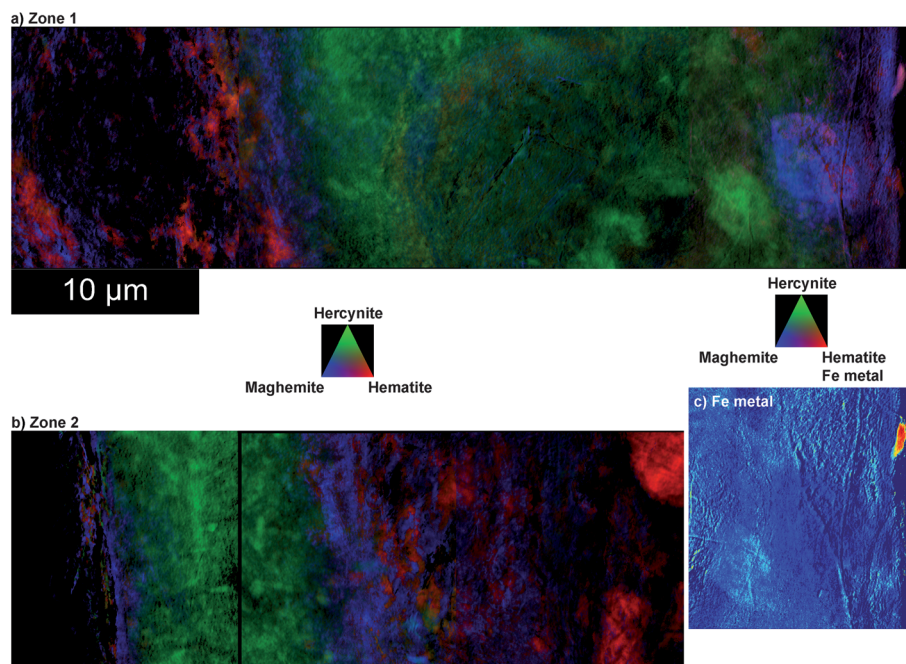


**Fig. 5** Final phase maps obtained from the least squares linear combination fit of reference XANES for hercynite, hematite, and maghemite to each single pixel XANES of zone 1 (a) and zone 2 (b) of the Pre-sigillata sample. The surface area of zone 1 was fitted using an additional reference XANES for metallic Fe, because a small Fe metal particle was identified at the surface. To separate hematite and Fe metal, both represented by the red color in the RGB phasemap of the surface tile of the mosaic map, the distribution of Fe metal is displayed in (c). (Data collected at SSRL beamline 6-2c; FOV zone 1:  $3478 \times 929$  pixels or  $48.34 \times 12.91 \mu\text{m}^2$ , binning 2; FOV zone 2:  $2579 \times 912$  pixels or  $35.84 \times 12.68 \mu\text{m}^2$ , binning 2.)

body. The results of a LSLC fitting to the XANES of the clusters using hercynite and maghemite are reported in Table 3 and Fig. 8. Based on these results the final phase map (Fig. 6d) was created by LSLC fitting of each single pixel XANES using the reference XANES for hercynite and maghemite.

The Fe valence front clearly suggests oxidation of the sample from the body to the slip. This is especially evident at the small crack in the slip extending from the body to the surface region of the slip (upper central part of the sample; Fig. 6 and 7), where the trivalent Fe (maghemite) phase is present throughout the length of this 'channel' but the trivalent phase is confined to near the surface of the crack and does not extend into the core of the slip. Confinement of the trivalent phase to regions near open channels suggests that the re-oxidation is controlled by diffusion of oxygen and, therefore, the porosity of the sample is the key variable influencing the (re)oxidation of the hercynite phase.

This hypothesis was further investigated by performing X-ray tomography (*cf.* Section 3.2.3) of the volume including the crack to establish a quantitative analysis of the sample porosity. This

region of the whole reconstructed volume was rendered and is displayed in Fig. 9.

The porosity (or void fraction, defined as the ratio of void over total volume) of this region was calculated as a function of depth from the surface into the body of the sample. Accordingly, the "Fe porosity", was determined from the 3D Fe distribution, indicating the correlation between the Fe concentration and the total solid material. In order to correlate porosity with the (2D) chemical information displayed in Fig. 6d, the reconstructed volume was registered with the corresponding area in the chemical phase map (Fig. 10a).

Fig. 10b shows the evaluated region of the phase map (black frame) and 3D data (red frame) together with the plots for porosity (dotted lines) and chemical phase (solid lines) as a function of depth from the surface into the body of the sample. The chemical phase percentage in this plot was calculated as the average percentage of all pixels in each image column (which sums to 100% when adding both phases). This correlation of porosity and chemical phase is possible because (i) both



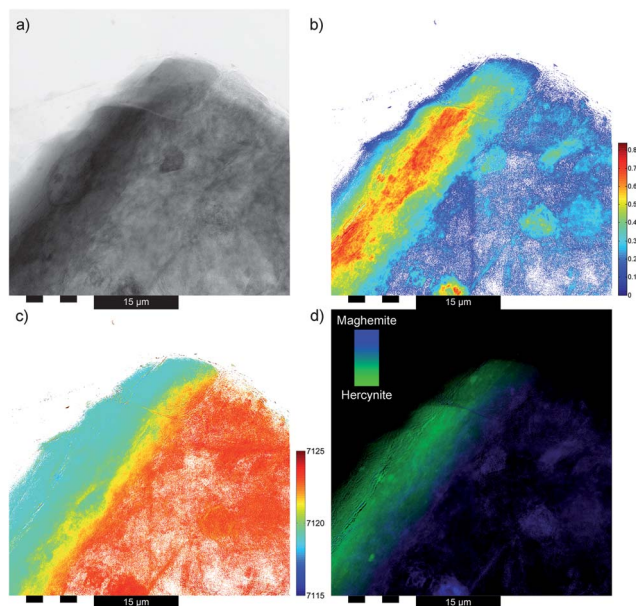


**Fig. 6** (a) Transmission image recorded for the sample CABnrb-B at 7225 eV, i.e., above the Fe absorption edge. The data was collected at SSRL beamline 6-2c in mosaic mode putting together 4 ( $2 \times 2$ ) partly overlapping images with a FOV of  $29.2 \times 29.2 \mu\text{m}^2$  resulting in a total FOV of  $49.7 \times 50.6 \mu\text{m}^2$  ( $1743 \times 1777$  pixels, binning 2). The edge-jump map (corresponding to the Fe concentration) as well as the edge energy map (correlated to the Fe valence) are displayed in (b) and (c), respectively. The final phase map obtained from a least squares linear combination fit of reference XANES for hercynite and maghemite to each single pixel XANES is shown in (d). The scale bar for (b) reports the values of the (absorption) edge jump, defined as the difference between the average intensity value in the XANES post-edge region and the average intensity value in the XANES pre-edge region. The scale bar for the map shown in (c) indicates the energy of the (absorption) edge in eV.

chemical phase and porosity plots represent an average over depth and the vertical axis of the sampled volume (as shown in Fig. 10b) and (ii) the separation between slip and body is quite well aligned in depth. It is interesting to note that the change in porosity which indicates the transition from the dense slip to the more porous body takes place within 3–4 microns (at the depth of  $\sim 14$  to  $\sim 17 \mu\text{m}$  from the surface) while the phase transition starts earlier at about  $7 \mu\text{m}$  depth and extends over *ca.*  $9 \mu\text{m}$  to a depth of  $16 \mu\text{m}$ . This indicates that the re-oxidation of the slip must have started from the porous body and then extended towards the surface. The 3D data shows possible pathways for fast transport of oxygen through micro-cracks and open micropores to oxidize the ceramic next to these channels, quickly converting Fe minerals from hercynite to maghemite, and then slowly diffusing through the denser slip to push the re-oxidation front deeper into the slip. The depth of this re-oxidation front from the open channel into the slip is therefore a measure of the temperature and time of the re-oxidation phase.

**4.2.2 Full-field XANES at ESRF: comparison and complementary analysis.** A second thin cross-section was prepared from the same Campanian sherd. This sample was also analysed by Full-Field TXM but at the ESRF (*cf.* Section 3.3). The same data processing was used and the results are shown in Fig. 11 and 12. The huge FOV of the full-field XANES

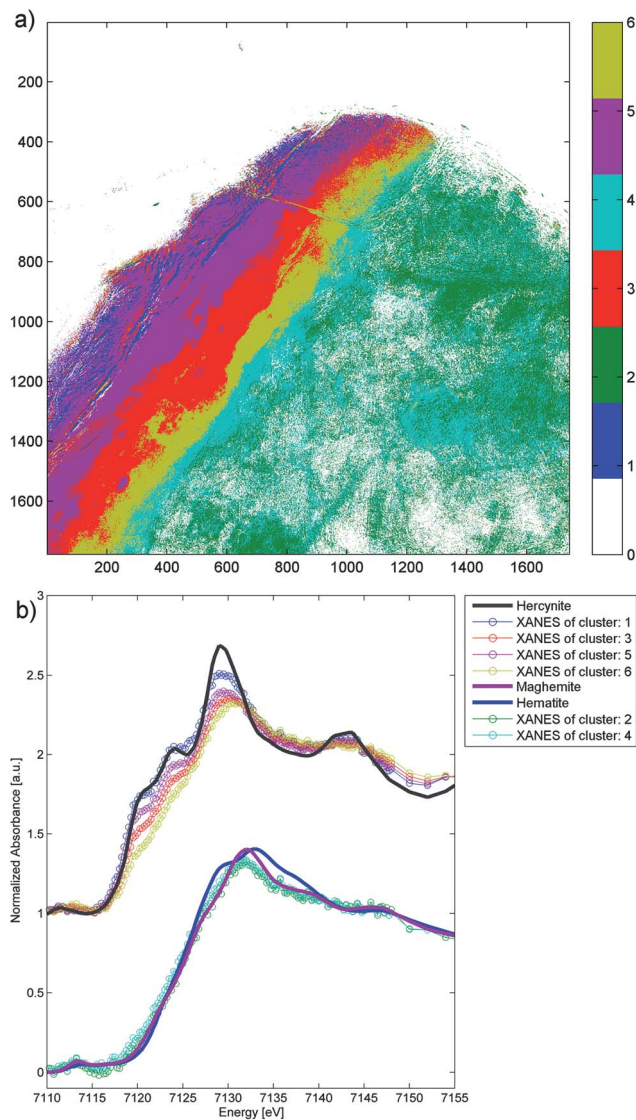


**Fig. 7** (a) Result of the image segmentation based on PCA and *k*-means clustering of the data set recorded for the sample CABnrb-B. The average XANES of each cluster is displayed in (b) together with reference XANES for hercynite and maghemite. (Data collected at SSRL beamline 6-2c, FOV:  $1743 \times 1777$  pixels or  $49.7 \times 50.6 \mu\text{m}^2$ , binning 2.)

**Table 3** Least squares linear combination fit results for clusters 1–6 from PCA and *k*-means clustering of the data collected for sample CABnrb-B (Fig. 7 and 8). Clusters have been sorted according to increasing maghemite concentrations

	Hercynite	Maghemite	<i>R</i> -square	<i>R</i> -factor	Reduced chi-square
Clt 1	0.92 (2)	0.08 (2)	0.457	0.003	0.0024
Clt 5	0.72 (2)	0.28 (2)	0.359	0.002	0.0019
Clt 3	0.56 (1)	0.45 (1)	0.248	0.002	0.0013
Clt 6	0.36 (1)	0.64 (1)	0.162	0.001	0.0009
Clt 4	0.13 (1)	0.87 (1)	0.109	0.001	0.0006
Clt 2	0.03 (1)	0.97 (1)	0.204	0.002	0.0011

configuration at ID21 is thoroughly adapted to the analytic task and mosaic mode was not required.

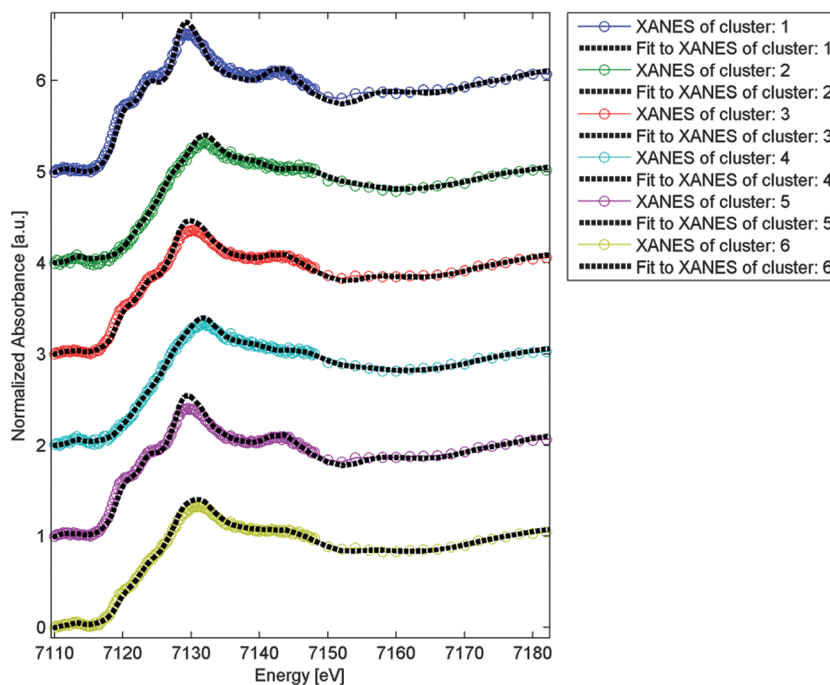


**Fig. 8** Result of a least squares linear combination fit of reference XANES for hercynite and maghemite to the XANES of clusters 1–6 resulting from PCA and *k*-means clustering of the data recorded for sample CABnarb-B.

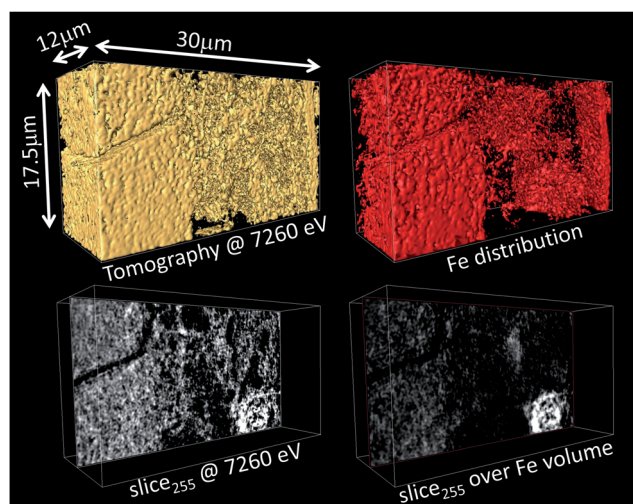


**Fig. 9** Top: reconstructed and rendered sub-volume of CABnarb-B, which includes the crack in the slip. Bottom: selected slices of the volume showing the distribution of total material (left) and Fe only (right).

Although the spatial resolution is lower (about one order of magnitude) than the one offered by the TXM at SSRL, the main features can still be very easily extracted from this map. The spatial resolution is sufficient to see the localized patches of oxidation at the surface of the slip (Fig. 11d) and both the high concentration of hercynite in the slip as well as the massive presence of maghemite in the body are clearly visible (Fig. 12). Without the colossal field of view, sufficiently high spatial resolution, and exquisite mineralogical sensitivity of the ESRF XANES full-field microscope, it would be impossible to reliably

detect the very heterogeneous and shallow oxidation of the surface of the slip. Furthermore, it was possible to detect small islands of hematite and a few islands of hercynite in the body. These small islands of hematite in the body and thin patches of maghemite at the surface were confirmed by spot analysis using micro-Raman spectroscopy (Fig. 12b–d). The Raman peaks at 227, 247, 293, 411, 500, 615 and 1326  $\text{cm}^{-1}$  are characteristic for the hematite spectrum while the doublet at 677–727  $\text{cm}^{-1}$  is the main characteristic peak for maghemite.<sup>29</sup> Optical observation revealed that the body of these Campanian ceramics contains a few large hematite crystals (5–20  $\mu\text{m}$ ). One of these crystals appears in the analyzed area. The iron concentration is very high in these large crystals, leading to a strong X-ray absorption, which results in very low transmission and poorer quality XANES. For these few regions with very high Fe concentration LSLC fitting of the XANES is problematic and misleading (see Fig. 12), however, micro-Raman spectroscopy for these regions is not affected by the large Fe concentration and very well complements XANES measurements (Fig. 12c).

For moderately noisy XANES data, caused by low Fe concentrations, the difference between pure magnetite and an equal proportion mixture of hercynite/hematite or hercynite/maghemite is often not detectable making the identification of small amounts of magnetite difficult. Again, micro-Raman spectroscopy is complementary in this case and can easily distinguish magnetite from hematite. On the other hand, in Raman spectroscopy hercynite can be difficult to identify.<sup>30</sup> Even in the slip where the concentration of hercynite is high, we were not able to obtain an unambiguous Raman spectrum. However, the successful combination of the two complementary



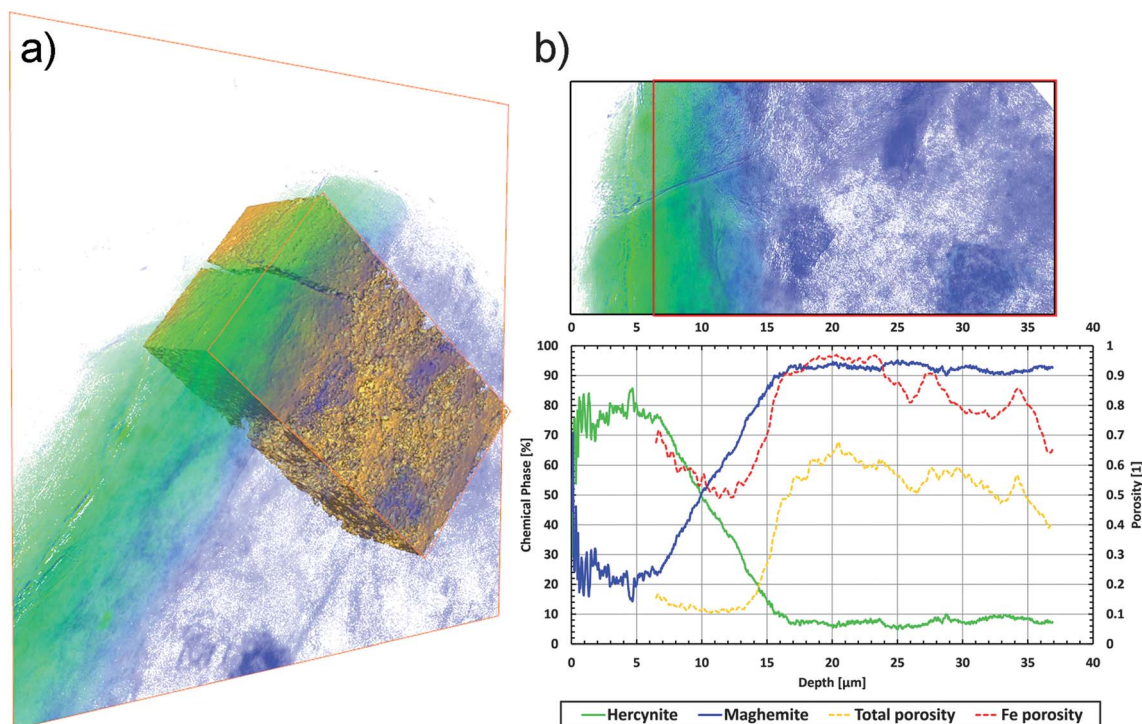


**Fig. 10** (a) Registration of the 3D tomographic data with the 2D mosaic phase map; (b) Evaluated area of the 2D phase map (black frame) and 3D data (red frame) together with the corresponding plots of the porosity and chemical phase as a function of depth from the sample's surface (slip) into the body.

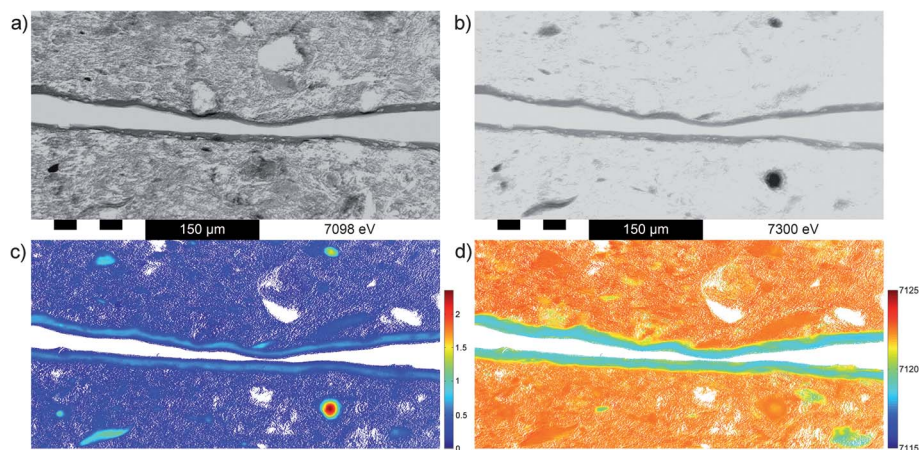


**Fig. 11** Transmission images recorded for the CABNarb-D sample at the ID21 beamline at the ESRF. (a) image recorded at 7098 eV, *i.e.*, below the Fe absorption edge and (b) image recorded at 7300 eV, *i.e.*, above the Fe absorption edge (FOV: 2032 × 1036 pixels or 610 × 311 μm<sup>2</sup>, pixel size 300 nm). The edge-jump map corresponding to the Fe concentration as well as the edge energy map correlated to the Fe valence are displayed in (c) and (d), respectively. The scale bar for (c) reports the values of the (absorption) edge jump, defined as the difference between the average intensity value in the XANES post-edge region and the average intensity value in the XANES pre-edge region. The scale bar for the map shown in (d) indicates the energy of the (absorption) edge in eV.

methods allows unequivocal identification of hercynite and magnetite, and this approach allowed us to detect small quantities of both hercynite and magnetite in the body.

Furthermore, another excellent example of the power of statistical analysis made possible by the extremely large number of measured XANES is seen when the quality of the LCLS fit (*R*-factor commonly used in XANES analysis<sup>27</sup>) for each pixel is plotted against the value of the edge-jump *versus* for that pixel.

Such a statistical correlation map clearly reveals that some pixels with similar edge-jump have significantly larger *R*-factor (Fig. 13a).

These anomalous pixels have manually been clustered (cluster 3, red), and for comparison pixels showing *R*-factors above ~0.025 (cluster 2, green). The pixels in cluster 2 (green) are homogeneously distributed in the cluster map of the sample and the larger *R*-factor simply reflects the much higher statistical noise corresponding to weakly absorbing areas in



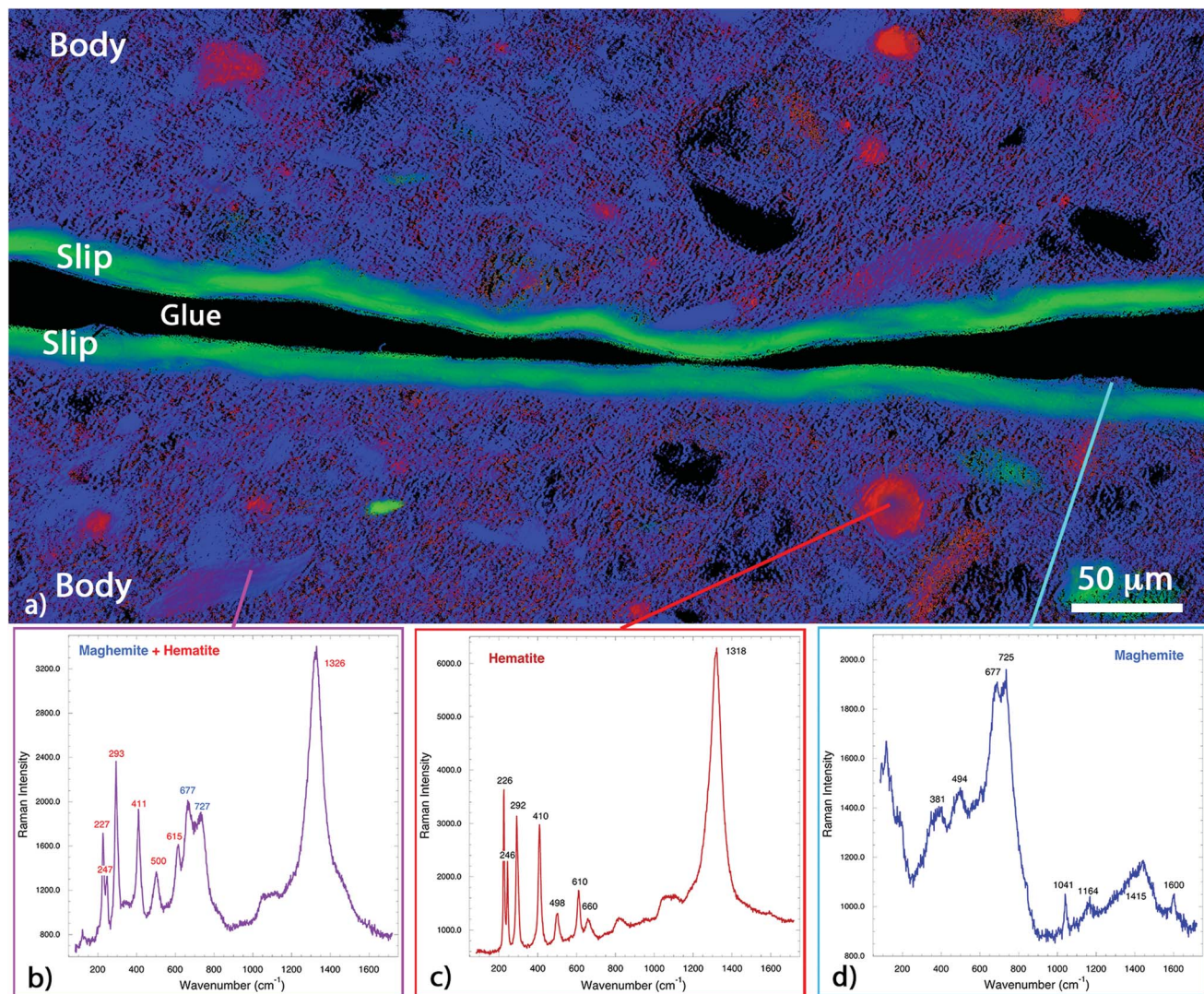


**Fig. 12** (a) Phase map deduced from measurements performed at ID21 (ESRF) including Raman spectra recorded at various points (b–d). Hercynite (green), maghemite (blue) and hematite (red), FOV: 2032 × 1036 pixels or 610 × 311 μm<sup>2</sup>, pixel size 300 nm.

the sample (low edge-jump values), and are not significant for a complete picture of the final phase map. On the other hand, the red pixels (cluster 3) highlight a distinct area of the sample (Fig. 13b), and suggest a particle with a phase not included in LCLS analysis. By comparing the average XANES of all pixels in cluster 3 with reference XANES for hercynite, maghemite, hematite, and almandine in Fig. 13c, it is clear that this particle contains a significant portion of a different Fe phase from the rest of the sample and is very possibly almandine. In Fig. 13d the result of a LSLC fit to the XANES of cluster 3 using the above mentioned set of references is displayed. The corresponding phase fractions and the quality of fit parameters are reported in Table 4. The much improved *R*-factor lends confidence to the assertion that cluster 3 indeed highlights a tiny almandine particle embedded within the ceramics body dominated by maghemite. Almandine belongs to the garnet group and is the most common species of this mineral group.<sup>31</sup> Garnets are particularly characteristic of metamorphic rocks and it is rare to find them in ceramic body.

However, garnets are also present as detrital grains in sediments and can be present in small amounts in raw clay used to make the ceramic body. Furthermore, almandine is stable under reducing atmosphere in the temperature range of ceramic firing (<1100 °C). Its presence in the fired ceramic body suggests that the reducing phase of the three step firing did not exceed 1100 °C, and the re-oxidation stage of the firing sequence was not sufficiently high in temperature or long in duration to oxidize it to Fe<sup>3+</sup> (and thus decompose it to hematite).

This result again nicely exemplifies the power of our approach to reliably find and identify a unique, very small area within a large FOV, in this case a region consisting of ~400 pixels within a total area of more than 2.1 million pixels or, in other words, detection of a secondary phase that occupies less than 0.02% of the total volume of the sample.

Finally, a few micro X-ray diffraction (XRD) patterns from the surface of the slip of the Pre-sigillata sample were recorded in Bragg-Bretano geometry. A typical XRD result, reported in

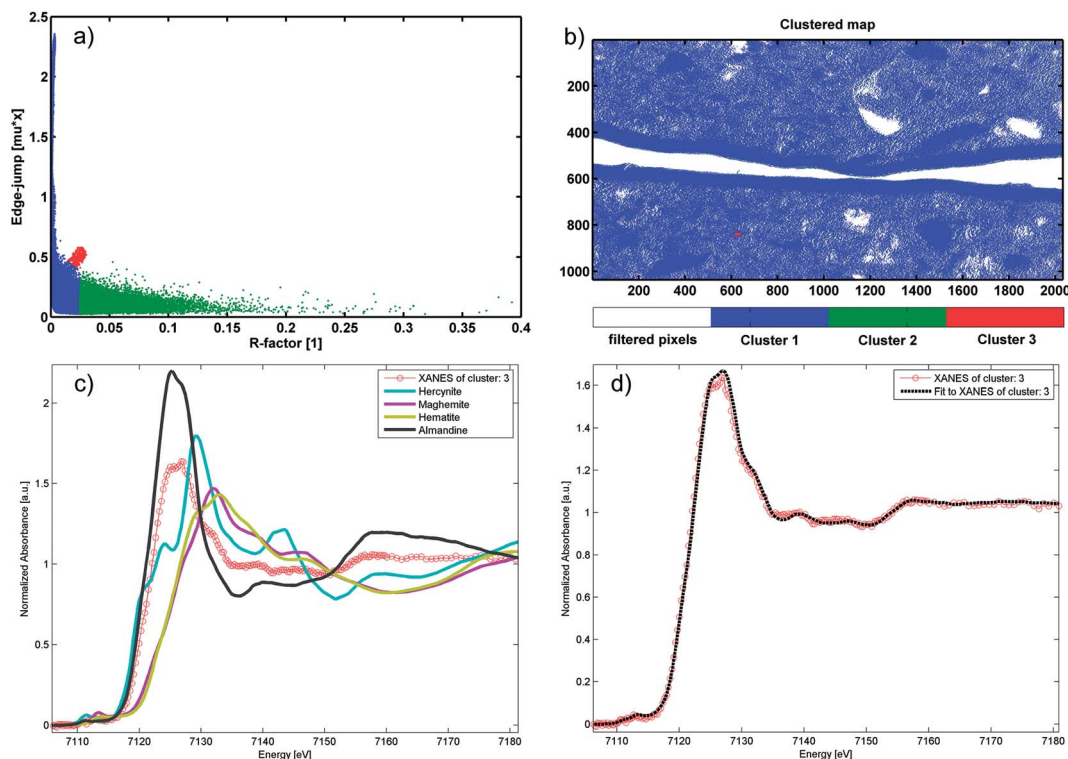


**Fig. 13** (a) Edge-jump versus *R*-factor correlation analysis showing the manual clustering of pixels with an *R*-factor larger than pixels of similar edge-jump (red) as well as pixels with *R*-factor larger than  $\sim 0.025$  (green). In (b) the resulting image segmentation based on the clustering performed in the correlation plot is displayed, and (c) compares the average XANES of each cluster with reference XANES for hercynite, maghemite, hematite and almandine. In (d) the result of a LSLC fit to the XANES of cluster 3 using these references is reported. (Data collected at ID21 (ESRF), FOV:  $2032 \times 1036$  pixels or  $610 \times 311 \mu\text{m}^2$ , pixel size 300 nm.)

**Table 4** Least squares linear combination fit result for cluster 3 of the edge-jump versus *R*-factor correlation analysis of the data collected at the ESRF for the Campanian sample (Fig. 13)

	Hercynite	Maghemite	Hematite	Almandine
Cl 3	0.018 (8)	0.379 (34)	0.000 (34)	0.603 (4)
	<i>R</i> -square	<i>R</i> -factor	Reduced chi-square	
Cl 3	0.1323	0.0004	0.0003	

Fig. 14, shows three spinel phases (hercynite, magnetite and maghemite), plus quartz and feldspar, but no hematite, confirming the combined XANES and Raman results. The absence of hematite is the main difference between the XRD measurements reported here from those reported for the Pre-sigillata (PTSGD17-H) published in Fig. 3 of ref. 16. (Though the XRD pattern of sample PTSGD17-H is not shown in ref. 16, but as mentioned in the text of ref. 16, the PTSGD17-H and PTSGD17-C samples have the same elementary and mineral compositions.) Maghemite was not reported for this Pre-sigillata in ref. 16. However the main peak of maghemite ( $35.64^\circ 2\theta$ ) is nearly coincident with a strong peak of hematite ( $35.68^\circ 2\theta$ ) and one cannot exclude its presence in XRD measurements when a significant amount of hematite is present.

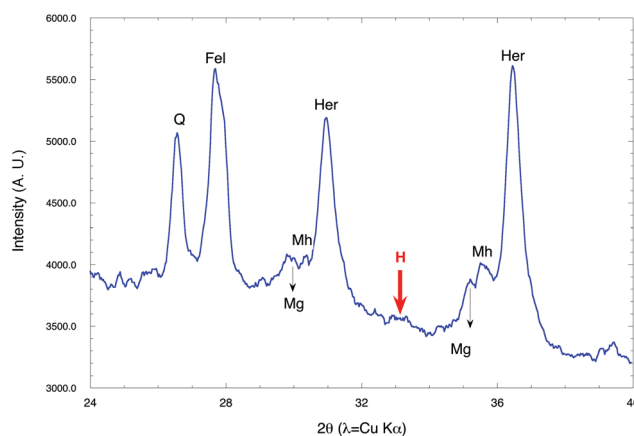


**Fig. 14** XRD pattern recorded at the slip surface of the CABNarb-B sample. Q: quartz, Fel: feldspar, Mg: magnetite, Mh: maghemite, Her: hercynite and H: hematite.

## 5. Conclusions

In the case of the two Roman ceramics investigated here the distribution of all three mineral phases of Fe, namely hercynite (black,  $\text{Fe}^{2+}$ ), hematite, and maghemite (both red,  $\text{Fe}^{3+}$ ), are important, but the distribution of maghemite, especially its phase boundaries with hercynite and hematite show the clearest difference between the two and give the clearest insights into the firing conditions the two vessels must have experienced.



Maghemite is an oxidized mineral of Fe with a spinel like structure. It can be produced either by severe and prolonged shear stressing of hematite,<sup>32</sup> or as an intermediate phase during moderate temperature oxidation of reduced Fe spinels, such as magnetite or hercynite. (At moderate temperature, oxidation of a reduced Fe spinel first converts all the bivalent Fe to trivalent Fe and thus forms maghemite, which then slowly transforms to hematite.<sup>33–35</sup>) It can be assumed that maghemite in these ceramics comes predominantly from oxidation of hercynite or magnetite, and not from prolonged shear deformation.

The distribution of maghemite at the interface of slip and body and the outside surface in both sherd types (Pre-sigillata and Campanian), especially the tendril like incursion visible in the SSRL data from oxidized to reduced areas, presents a compelling and very pictorial evidence that these vessels were once reduced and then partially re-oxidized. A relatively uniform hercynite slip and a very thin or nearly absent oxidation layer on the surface indicates that the producers of this vessel were able to successfully re-oxidize the body to Fe<sup>3+</sup> while preventing the slip for re-oxidizing. This remarkable achievement, often not achieved in modern replications, suggests that the creators of these vessels possessed sufficient technical knowledge to be able to control the porosity of this hierarchically complex object at multiple lengths through sophisticated manipulation of clay chemistry and morphology and kiln firing conditions. Furthermore, the distribution of the maghemite phase points to two interesting differences between the two types of Roman black gloss sherds investigated here. The first distinction is the very patchy and, when present, very thin oxidation layer on the surface of the Campanian slip in comparison to a thicker and more uniform layer on the Pre-sigillata slip. The very thin and patchy surface oxidation layer on the Campanian vessel, as opposed to a relatively uniform and continuous layer on the Pre-sigillata vessel, suggests that either the surface layer was polished away after firing (either intentionally by the potter or worn away over the last 2000 years), or that the surface of the slip was protected from oxygen during re-oxidation and the vessel oxidized from the inside out.

The second difference is perhaps more significant. Intriguingly, the body of the Pre-sigillata appears to be mostly hematite whereas that of the Campanian is mostly maghemite with a few large islands of hematite centered on large embedded crystals.

The large amount of maghemite in the body of the Campanian ceramic, when added to the presence of a significantly thinner surface oxidation (maghemite) layer, and presence of patches of un-oxidized Fe<sup>2+</sup> minerals in the body (the large Almandine particle, and small patches of hercynite) suggests that the final re-oxidation step of the three stage firing protocol for the Campanian ceramic was performed under either lower oxygen fugacity or even more likely at significantly lower temperature and/or shorter duration than the Pre-sigillata ceramic.

In conclusion, we believe that the two examples in here demonstrate that identification of the mineralogical phases and mapping their distribution (in conjunction with porosity) at relatively fine scale over very large areas can lead to profound new insights into the production processes and functioning of hierarchically heterogeneous materials.

## Acknowledgements

Some of the measurements reported in here were performed on beamline 6-2c at the Stanford Synchrotron Radiation Light-source, a Directorate of SLAC National Accelerator Laboratory and an Office of Science User Facility operated for the U.S. Department of Energy Office of Science by Stanford University. Other measurements were performed on beamline ID21 at the European Synchrotron Radiation Facility (ESRF), Grenoble, France. The authors would also like to thank Alain Vernhet for La Graufesenque archaeological samples as well as Nicolas Ratel-Ramond for technical support during X-ray diffraction measurements.

## Notes and references

- 1 M. S. Tite, *Archaeometry*, 2008, **50**, 216–231.
- 2 J. V. Noble, *The techniques of painted Attic pottery*, New York, 1965.
- 3 M. S. Tite, M. Bimson and I. C. Freestone, *Archaeometry*, 1982, **24**, 117–126.
- 4 T. Pradell, J. Molera and M. Vendrell-Saz, *Hyperfine Interactions*, 2002.
- 5 M. S. Walton, E. Doehne, K. Trentelman, G. Chiari, J. Maish and A. Buxbaum, *Archaeometry*, 2009, **51**, 383–396.
- 6 P. Sciau, Y. Leon, P. Goudeau, S. C. Fakra, S. Webb and A. Mehta, *J. Anal. At. Spectrom.*, 2011, **26**, 969–976, DOI: 10.1039/c0ja00212g.
- 7 P. Sciau, S. Relaix, C. Roucau and Y. Kihn, *J. Am. Ceram. Soc.*, 2006, **89**, 1053–1058.
- 8 J. C. Andrews, E. Almeida, M. C. H. van der Meulen, J. S. Alwood, C. Lee, Y. J. Liu, J. Chen, F. Meirer, M. Feser, J. Gelb, J. Rudati, A. Tkachuk, W. B. Yun and P. Pianetta, *Microsc. Microanal.*, 2010, **16**, 327–336.
- 9 F. Meirer, J. Cabana, Y. J. Liu, A. Mehta, J. C. Andrews and P. Pianetta, *J. Synchrotron Radiat.*, 2011, **18**, 773–781.
- 10 J. C. Andrews, F. Meirer, Y. J. Liu, Z. Mester and P. Pianetta, *Microsc. Res. Tech.*, 2011, **74**, 671–681.
- 11 V. De Andrade, J. Susini, M. Salome, O. Beraldin, C. Rigault, T. Heymes, E. Lewin and O. Vidal, *Anal. Chem.*, 2011, **83**, 4220–4227.
- 12 B. Fayard, E. Pouyet, G. Beruyer, D. Bugnazet, C. Cornu, M. Cotte, V. De Andrade, F. Di Chiaro, J. Kieffer, T. Martin, E. Papillon, M. Salomé and A. V. Solé, *J. Phys.: Conf. Ser.*, 2013, **425**, DOI: 10.1088/1742-6596/425/19/192001.
- 13 M. Picon, in *Céramiques de la Graufesenque et autres productions d'époque romaine, hommages à Bettina Hoffmann*, ed. M. Genin and A. Vernhet, éditions monique mergoil, Montagnac, 2002, vol. 7, pp. 139–163.
- 14 D. Schaad, *La Graufesenque (Millau, Aveyron), volume I: Condatomagos une agglomération de confluent en territoire rutène*, 2007.
- 15 M. Genin and A. Vernhet, in *Céramiques de la Graufesenque et autres productions d'époque romaine, hommages à Bettina Hoffmann*, ed. M. Genin and A. Vernhet, éditions monique mergoil, Montagnac, 2002, vol. 7, pp. 105–132.



- 16 C. Mirguet, C. Dejoie, C. Roucau, P. de Parseval, S. J. Teat and P. Sciau, *Archaeometry*, 2009, **51**, 748–762.
- 17 J. Ayache, L. Beaunier, J. Boumendil, G. Ehret and D. Laub, *Guide de préparation des échantillons pour la microscopie électronique en transmission*, tome 2, PUSE, Saint-Etienne, 2007.
- 18 I. D. Gonzalez-Jimenez, K. Cats, T. Davidian, M. Ruitenbeek, F. Meirer, Y. J. Liu, J. Nelson, J. C. Andrews, P. Pianetta, F. M. F. de Groot and B. M. Weckhuysen, *Angew. Chem., Int. Ed.*, 2012, **51**, 11986–11990.
- 19 Y. J. Liu, F. Meirer, P. A. Williams, J. Y. Wang, J. C. Andrews and P. Pianetta, *J. Synchrotron Radiat.*, 2012, **19**, 281–287.
- 20 V. A. Sole, E. Papillon, M. Cotte, P. Walter and J. Susini, *Spectrochim. Acta, Part B*, 2007, **62**, 63–68.
- 21 I. T. Jolliffe, *Principal Component Analysis*, Springer-Verlag, New York, 2nd edn, 2002.
- 22 J. E. Jackson, *A User's Guide to Principal Components*, Wiley, Chichester, 2003.
- 23 U. Boesenberg, F. Meirer, Y. J. Liu, A. K. Shukla, R. Dell'Anna, T. Tyliczszak, G. Y. Chen, J. C. Andrews, T. J. Richardson, R. Kostecki and J. Cabana, *Chem. Mater.*, 2013, **25**, 1664–1672.
- 24 J. B. MacQueen, *presented in part at the Proceedings of 5-th Berkeley Symposium on Mathematical Statistic and Probability*, Berkeley, 1967.
- 25 R. A. Johnson and D. W. Wichern, *Applied multivariate analysis*, Pearson, Upper Saddle River, NJ, 5th edn, 2002.
- 26 Y. J. Liu, F. Meirer, J. Y. Wang, G. Requena, P. Williams, J. Nelson, A. Mehta, J. C. Andrews and P. Pianetta, *Anal. Bioanal. Chem.*, 2012, **404**, 1297–1301.
- 27 B. Ravel and M. Newville, *J. Synchrotron Radiat.*, 2005, **12**, 537–541.
- 28 M. Newville, B. Ravel, D. Haskel, J. J. Rehr, E. A. Stern and Y. Yacoby, *Physica B*, 1995, **208**, 154–156.
- 29 F. Froment, A. Tournié and P. Colomban, *J. Raman Spectrosc.*, 2008, **39**, 560–568.
- 30 Y. Leon, C. Lofrumento, A. Zoppi, R. Carles, E. M. Castellucci and P. Sciau, *J. Raman Spectrosc.*, 2010, **41**, 1550–1555.
- 31 W. A. Deer, R. A. Howie and J. Zussman, *An introduction to the rock-forming minerals*, Pearson, Harlow, 1992.
- 32 E. Petrovsky, V. Kropacek, M. J. Dekkers, C. deBoer, V. Hoffmann and A. Ambatiello, *Geophys. Res. Lett.*, 1996, **23**, 1477–1480, DOI: 10.1029/96gl01411.
- 33 G. Menegazzo and S. Carbonin, *Phys. Chem. Miner.*, 1998, **25**, 541–547, DOI: 10.1007/s002690050146.
- 34 F. Bourgeois, P. Gergaud, H. Renevier, C. Leclere and G. Feuillet, *J. Appl. Phys.*, 2013, **113**(1), 013510, DOI: 10.1063/1.4772714.
- 35 P. S. Sidhu, *Clays Clay Miner.*, 1988, **36**, 31–38, DOI: 10.1346/ccmn.1988.0360105.